Imaging of the Temperature Distribution in a Catalyst Test Chamber using Laser Rayleigh Scattering

Sebastian Pfaff

5th February 2015

Abstract

In order to accurately measure the effect on the gas concentration around catalysts in a high pressure environment using laser based techniques such as Laser Induced Florescence (LIF), accurate temperature maps of the test chamber used are required. In order to create such temperature maps Laser Rayleigh Scattering (LRS) is utilized which allows for a non-intrusive probing of temperatures in a two dimensional measurement area. We have created temperature maps for pressures of interest (100 mbar, 500 mbar, 900 mbar) for past and future catalyst measurements at various flows (100 ml/min, 500 ml/min, 900 ml/min). We also discuss the accuracy of these measurements and the usefulness of the data for the calibration of future concentration measurements.

LUND
UNIVERSITY

Division of Combustion Physics
Department of Physics

Supervised by Johan Zetterberg and Jianfeng Zhou

January, 2015

Lund Reports on Combustion Physics, LRCP-182
ISRN LUTFD2/TFCP-182-SE
ISSN 1102-8718
Lund, Sweden, January 2015
Sebastian Pfaff
Division of Combustion Physics
Department of Physics
Lund University
P.O. Box 118
S-221 00 Lund, Sweden

Contents

List of Abbreviations

STM Surface Tunnelling Microscopy

LEED Low Energy Electron Diffraction

MS Mass Spectroscopy

LIF Laser Induced Fluorescence

LRS Laser Rayleigh Scattering

SLIPI Structured Laser Illumination Planar Imaging

Nd:YAG Neodymium-Doped Yttrium Aluminium Garnet

MFC Mass Flow Controller

ESRF European Synchrotron Radiation Facility

1 Introduction

The study of the catalytic properties of metals is vital to broaden our understanding of the chemical processes involved as well as steering the development of new catalysts into the right direction [1, 2]. Since the chemical reactions occur on the surfaces of the catalyst, much effort has been directed to investigating the surface structure of catalysts using techniques such as surface tunnelling microscopy (STM) or low energy electron diffraction (LEED) with which the surface structure is investigated [3]. The use of these techniques, however, is usually limited to the ultra high vacuum pressure range at around 10^{-9} mbar. This means the catalyst is investigated in conditions where it is not normally operating. Normal operation usually implies a pressure of approximately 1 bar and a gas flow around the catalyst with which the catalyst surface interacts. For this reason STM methods that allow operation at high pressures (1 bar) have been developed [4]. The availability of these techniques has called for a deeper investigation of the gas-catalyst interaction. It is therefore crucial to study the properties of catalysts and their surfaces at high pressure (1 bar) while exposed to a certain gas flow [4].

This may be accomplished by placing the catalyst to be investigated into a closed chamber which allows for the variation of gas flow, gas composition, pressure and catalyst temperature. Catalyst temperature variation is very important since catalysts have to be heated to a certain temperature in order to become active. The gas flowing out of the chamber is usually redirected to a mass spectrometer (MS) in order to gauge the concentration of the species contained in the gas [5, 6]. While this may provide a satisfactory picture of the total effect of the catalyst it does not provide any specific information about the gas concentration at specific points on or just above the catalyst surface. Even when using very small MS probes to investigate the gas species concentration in a certain point one MS-device is needed for every point to be investigated simultaneously making it impractical to investigate several points at once. Also, the MS-probes may disrupt the natural gas flow over in the chamber which provides for additional uncertainties.

Instead of MS, laser based techniques for measuring gas concentration can be used. A laser beam can be very accurately focused into the region of interest providing high spatial resolution ($\approx 50\,\mu m$). Laser Induced Florescence (LIF) is a laser based technique where the gas is excited by the laser beam and the fluorescence is measured [7]. Since the wavelength of the fluorescence is species-specific this can be used to probe the concentration of a specific species. Using LIF a two dimensional concentration map may be produced by using a cylindrical lens to focus the laser into a sheet. The fluorescence intensity within the region of interest is then imaged using a camera sensitive to the fluorescence wavelength for the species of which the concentration is to be gauged. The fluorescence intensity, however, is also dependent on temperature as lower temperature will cause a greater density and thus a higher fluorescence signal independent of the catalyst. This means the absolute accuracy of LIF is dependent on accurate temperature maps to be able to compensate for temperature induced intensity fluctuations. This paper will describe the temperature measurements.

Measuring temperature is traditionally done using thermal sensors such as thermistors or thermocouples placed in the point(s) of interest. These methods involving physical thermal probes inserted into the test chamber may similarly to the MS probes above disrupt flow. They may also alter the temperature and chemistry in the insertion point and make it difficult to perform measurements at multiple points simultaneously since very many probes would be required to obtain a good spatial resolution. Thus non-intrusive laser technique is strongly preferred in order to non-intrusively measure the temperature in two dimensions. Laser Rayleigh Scattering (LRS) is a technique which can be used to measure the spatial temperature distribution in gases [8]. The technique involves creating a laser sheet probing the gas in the region of interest and then imaging the Rayleigh scattered light from that area. Since the intensity of scattered light depends on the number of scatterers in that point it can be related to the temperature through the ideal gas law. However, as with all measurements involving Rayleigh scattering the technique has the drawback that the scattered light to be measured is emitted instantaneously and at the same wavelength as the incoming laser light. This property makes it difficult to filter away the background light caused by reflections in the setup. A setup involving a closed chamber further intensifies this problem since the chamber and its windows inevitably will increase the amount of reflections in the system. Two viable ways of solving the background problem may be attempted. Firstly, a technique called

Structured Laser Illumination Planar Imaging (SLIPI) has been developed where the intensity of the laser sheet used for the LRS measurement is striped horizontally by introducing a diffraction pattern [9]. This enables a post-processing subtraction of the background using frequency filtering at the cost of resolution. A more simple solution is to isolate and subtract the background. This is possible in our case since the test chamber used may be brought down to pressures where there is no significant scattering. This background is then subtracted from the data images.

Both regular LRS with simple background subtraction and background elimination using SLIPI were attempted. However it was determined that regular background subtraction proved to be efficient enough and so it was decided to avoid the additional layer of complexity, such as several lenses to create the striped interference pattern, which a SLIPI setup would have introduced.

We have measured the temperature in a catalyst reaction test chamber using LRS with background subtraction at several flows and pressures usually used for catalyst measurements [10]. Using the results of these measurements we have constructed temperature maps which can be used for the calibration and temperature correction of past and future measurements using the same chamber which will improve their accuracy and in extension our understanding of the inner workings of catalysts.

2 Method

2.1 Laser Rayleigh Scattering

Laser Rayleigh Scattering is a technique that may be used as a tool to measure temperature in isobaric environments. Intensity scattered light depends on the number of scatterers, the incoming laser intensity as well as the composition of the scattering gas according to

$$I = kNI_0 \sum_i \sigma_i c_i, \tag{1}$$

where k is a calibration constant, N is the total number of gas molecules in the volume to be investigated and I_0 is the initial laser intensity. The sum is a sum over all types of molecules where σ_i is the scattering cross section and c_i is the concentration of the ith gas in the mixture.

The Rayleigh scattering cross section for a certain gas may be written as [11]

$$\sigma = \frac{4\pi^2(n-1)^2}{\lambda^4 N_0^2} \sin^2\theta \epsilon_{i\lambda}, \tag{2}$$

where n is the index of refraction, N_0 is Loschmidt's number for the conditions of the index of refraction measurement, λ is the laser wavelength, θ is the angle between the incoming laser and the scattered light. $\epsilon_{i\lambda}$ is a factor dependent on the depolarisation ratio which in turn is dependent on the gas as well as λ. This factor however is considered to be negligible ($< 5\%$) for the wavelength used for these measurements [11]. The actual intensity of the scattering is then the integral over the angle of interest.

We now measure the two intensities, one at a known reference temperature I_r and the other I_u at an unknown temperature.

If we keep the same gas concentration and all other experimental parameters such as camera exposure time and laser pulse duration constant during both measurements the sum cancels and we are left with

$$\frac{I_r}{I_u} = \frac{I_{0r}N_r}{I_{0u}N_u}. \tag{3}$$

Assuming we may correct for the difference in initial laser energy this expression in combination with the ideal gas law $pV = kNT$ gives a direct relation to temperature between the two measurements.

$$\frac{I_r}{I_u} = \frac{I_{0r}p_rV_rT_u}{I_{0u}p_uV_uT_r} \tag{4}$$

For a fixed pressure $p = p_u = p_r$ and fixed volume $V = V_u = V_r$ things cancel and this expression gives that the amount of scatterers is inversely proportional to the temperature. Still, assuming we can correct for eventual laser energy differences we obtain

$$\frac{I_r}{I_u} = c_E \frac{T_u}{T_r}, \tag{5}$$

where c_E is a factor to correct for any laser energy difference.

By measuring the scattered light intensity at a known reference temperature as well as at an unknown temperature this may be used to deduce the unknown temperature. The accuracy of this method is dependent on how accurately laser energy differences can be compensated for as well as the accuracy of the intensity measurement.

The largest hurdle in this case is the fact that Rayleigh scattering is an instantaneous effect and the scattered light is of the same wavelength as the incoming light. This means there is no efficient way to separate the Rayleigh scattered light to be measured from all background scattering and reflections from the optical setup.

2.2 Optical setup

An optical setup was configured as presented in figure 1. The laser used was a Nd:YAG (Spectra Physics, PRO 290-10) which creates pulses with a wavelength of 532 nm by means of frequency doubling. Each pulse has a duration of 8 ns and an energy of around 750 mJ. However, due to the large number of apertures and mirrors in the setup the amount of energy that reaches the test chamber is significantly lower, around 150 mJ. The radius of the laser beam is around 3.5 mm. The laser is guided by a series of mirrors through a cylindrical lens which creates a thin laser sheet focused in the centre of the test chamber. The focal length the lens was 15 cm which allowed for a very thin laser sheet within the measurement area without focusing the laser too much as it passes through the chamber windows which only tolerate a limited amount of energy per area ($10\ \mathrm{J\,cm^{-2}}$). Assuming a perfectly Gaussian beam (which this is not) the beam width within the measurement area ranges from $w_0 \approx 14.5\,\mu\mathrm{m}$ at the beam waist to $w_1 \approx 327\,\mu\mathrm{m}$ at a distance of 0.7 cm from the waist [12, p. 157]. Even when allowing for a some error due to the beam waist not being perfectly in the middle of the measurement area and the fact that the beam will not be perfectly Gaussian the beam width will still be less than 0.5 mm. The temperature is not expected to vary much over that interval. Apertures were placed at various positions along the beam to reduce the amount of scattered light from things such as back reflections [13]. Much effort went into optimizing the setup in order to reduce background scattered light. This was done mainly using trial and error.

The beam continues through the test chamber and is redirected once more to reduce scattered light before it it dumped.

To measure the Rayleigh signal, an ICCD camera with a resolution of 1024×1024 px (Andor iStar USB) was used. The camera was pointed at the window parallel to the beam and was set up to trigger once each laser pulse. The influence of ambient light separate from the laser was eliminated by only integrating over around twice the laser pulse length where the laser pulse was centred in the integration time window.

2.3 Test Chamber

In the experiment a cube shaped test chamber with a volume of 23 cm^3 is used. The chamber has circular windows on three sides and one on top allowing for the laser to pass through two opposed windows while the experiment may be monitored through the top and side windows. In figure 2 a schematic view of the chamber is shown. For this experiment anti-reflection coated (at 532 nm) windows were chosen in order to reduce the scattered background light to acceptable levels. To further reduce background scatter the entire inside of the chamber (except for the windows) were coated with graphite. When referring to the chamber the front will henceforth be the side window used for observation.

The chamber also allows for flowing several types of gas through it. The gas inlet is near the bottom left, the outlet at the bottom right of the chamber. To regulate the gas flow individually

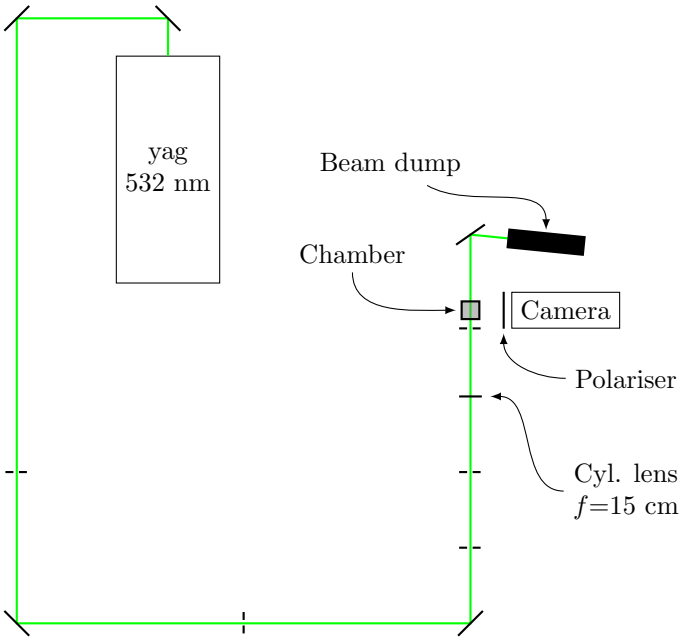

Figure 1: The optical setup used for the measurements. The large distance between laser and test chamber is due to the immobility of the laser and other setups in the lab. For closer view of the test chamber, see figure 2. The straight lines crossing the beam not labelled otherwise are the approximate locations of the apertures used to reduce background scattering.

for each gas, high precision mass flow controllers (MFCs) (Bronkhorst EL-FLOW) are used. The tubes through which the gas flows from the gas bottles to the chamber are around 5 m. With small flows of at most 250 ml/min the gas is thus assumed to have reached room temperature at the time it enters the chamber. For these measurements the only gases used were argon (Ar) and butane (C_4H_{10}).

Slightly below the middle of the chamber is a cross shaped heating plate (heating cross) the temperature of which is controlled by a heating current and measured by a thermocouple. Water cooling of the chamber edge with water at room temperature allows for a very precise relative temperature control. The accuracy of the absolute temperature value provided by the thermocouple is not known since the effect of the feed-through wires going into the vacuum introduce an unknown error. Nonetheless it will be used for the temperature adjustments. Also, a calibration curve for a similar thermocouple setup at the European Synchrotron Radiation Facility (ESRF) has been obtained. The measurements presented in this paper will then show the actual accuracy of the thermocouple and if it follows the calibration curve from ESRF. When measuring, the laser is aimed so that the lower edge of the sheet is about 5 mm above the heating cross. The distance is so large in order to minimize reflections from screws protruding from the heating cross securing the thermocouple and wires for the heating current.

2.4 Measurement

The measurements were done in series of increasing heating cross temperature. For every flow-pressure combination image series were produced at a heating cross temperature of 50 °C, 100 °C, 150 °C, 200 °C 250 °C and 300 °C. Also before and after each measurement a reference series at room temperature and a background with the chamber at vacuum ($\approx$ 2 mbar) were taken. Combinations of pressures and flows measured are shown in table 2.

Butane (C_4H_{10}) was chosen as the gas to use due to its comparatively large Rayleigh cross section of $\approx 132 \times 10^{28}$ cm^2, around 24 times larger than that of argon. This is necessary to be able to obtain a good data to noise ratio even for lower pressures such as 100 mbar where gases such as carbon dioxide or argon would have given very poor data. Table 1 shows the Rayleigh cross section calculated for some gases. Since the maximum flow of butane the MFCs could handle was

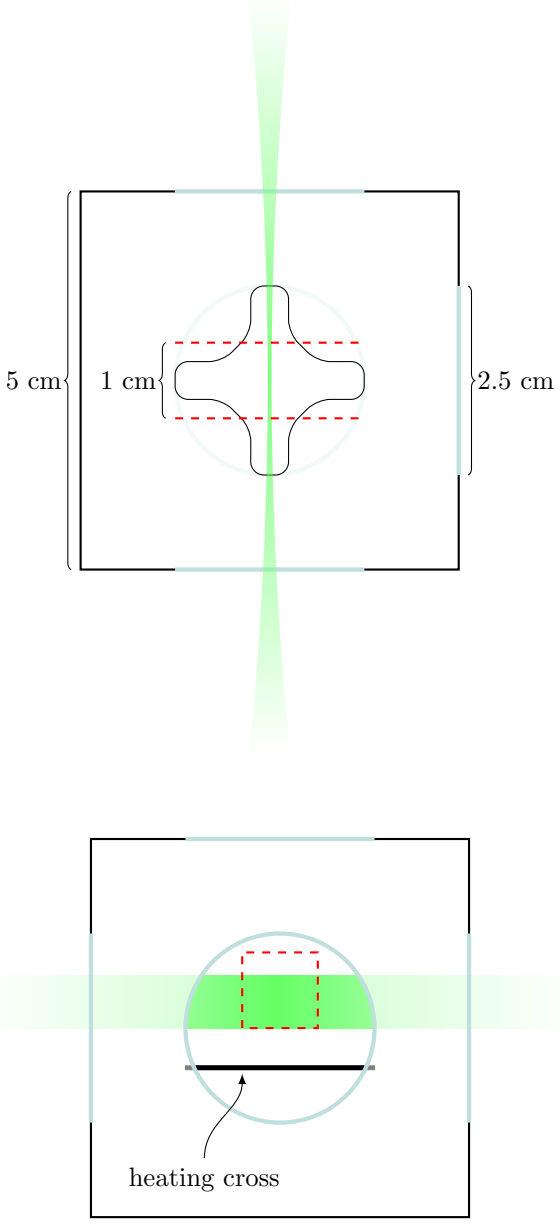

Figure 2: Schematic view of the test chamber from above (top) and from the front (bottom), the top view being rotated as figure 1. The laser sheet is shaded green, the camera view boundaries are dashed red. The width of the laser at the beam waist is around $\approx 14.5\,\mu m$

100 ml/min due to its heavy nature, argon (Ar) was flowed in addition to the maximum butane flow to archive the desired total flow. Each series consists of 2000 images for measurements at 100 mbar and 500 mbar and 1000 images for all measurements at 900 mbar. The number of images could be decreased due to the stronger signal at higher pressure. The camera produces images at a resolution of 1024×1024 px. However to be able to obtain a better signal to noise ratio, resolution was traded for additional signal by using 8×8 binning in the camera in order to gain more counts per pixel which decreases the per pixel readout noise. This also significantly decreased the readout time which enabled for larger image series.

2.5 Post processing

After the binning the final resolution of each image was 128×128 px. An average of all images in a series was used as final image for that temperature. Pixels outside the laser sheet, about the top third of the image, were cut away. Actual temperature maps were then produced by first subtracting the background from both reference and measurement images after which the reference is divided by the measurement image for the corresponding heating cross temperature. The resulting data is then multiplied by the temperature of the reference measurement in Kelvin.

The resulting images were then blurred with a 11 px mean filter. This was done since we were mostly interested in the temperature gradient. Furthermore, without blurring non-physical temperature variations from interference patterns in the optics were visible.

In order to obtain a mapping from pixels to actual space a 1×1 mm grid placed in the position of the laser sheet was photographed after the measurements with the same camera positioning. Each grid line was then mapped to a specific row of pixels. This provides a final spatial resolution in the x-y plane of 0.074 mm/px which of course is reduced somewhat by the mean filter.

3 Results

3.1 Temperature maps and plots

Some direct results from the LRS temperature measurements are presented in figures 4 to 7 where the distance d on the y-axis signifies millimetres above the heating plate and the distance x along the x-axis signifies millimetres left or right from the middle of the heating plate. The colors signify temperature as is shown in the color bars. Note that the value of the color bars changes between maps of different pressure. An overview of how flow, pressure and heating plate temperature affect the gas temperature in the blue rectangle at the bottom are given in figure 3. The rectangle location is chosen to be around 3.5 to 4.0 mm above the heating plate. This is the area we are the most interested in since it will be just above a potential catalyst crystal (1-2 mm high) placed on the heating plate. The temperature of this rectangle will henceforth be referred to as "rectangle temperature" (T_{rt}).

Table 1: Several Rayleigh cross sections σ calculated using (2) with $N_0 = 2.6867 \times 10^{25}\,\mathrm{m}^{-3}$ and $\lambda = 532\,\mathrm{nm}$. The indices of refraction n used in each calculation are also shown [14, part 8, pp. 6:871-889]. The values used for n are for $\lambda = 546\,\mathrm{nm}$, however, the difference between this and the $\lambda = 532\,\mathrm{nm}$ used in the experiment is considered to be negligible. Note the very large cross sections of the larger hydrocarbons.

Molecule	$(n-1) \times 10^6$	$\sigma \times 10^{28}/\mathrm{cm}^2$	$\sigma/\sigma_{\mathrm{Ar}}$
CO	336.2	7.72	1.42
CO_2	450.7	13.87	2.55
N_2	299.8	6.14	1.13
O_2	271.7	5.04	0.93
Ar	282.3	5.44	1.00
CH_4	443.3	13.42	2.46
C_3H_{10}	1102.1	82.93	15.24
C_4H_{10}	1390.1	131.94	24.25

Table 2: The flows measured at for each chosen pressure. For every flow temperatures between 50 °C and 300 °C were measured at in steps of 50 °C.

100 mbar	500 mbar	900 mbar
50 ml/min	50 ml/min	
100 ml/min	100 ml/min	100 ml/min
	250 ml/min	
		300 ml/min

The area shown in the temperature maps begins around 3.5 mm above the heating plate and extends to the top edge of the laser sheet around 11 mm above the heating plate while being aligned horizontally with the middle of the heating cross in the middle of the image. Figure 2 shows a visual representation of the area. The red frame in this figure represents the boundaries of the area imaged by the camera. In the post processing steps the top area, which is not part of the laser sheet, is cut away and thus the temperature maps show the area where the red dashed box and the green laser sheet overlap. In all images one can see the temperature increase towards the middle of the bottom edge which is the part closest to the middle of the heating cross.

The temperature trend plots to the right of the temperature maps show averages along the dashed rectangles, each point in the plot representing a horizontal average of the temperatures within the correspondingly coloured box at a height above the heating plate. A larger separation between the lines signifies a larger difference between the right, middle and left side temperatures. A larger variation of one plot signifies a larger difference between the top and bottom of the measurement area. For example the bottom trend plot in figure 7 shows a large left-right difference whereas the bottom image in figure 5 shows a large temperature difference between the top and bottom of the measurement area. A discussion of possible causes of these differences and other interesting traits of the temperature data follows below. The images taken at 50 °C steps were omitted due to reasons discussed below, the images taken at 150 °C and 250 °C were omitted due to space constraints but look as expected.

4 Discussion

The goal of this series of measurements was to provide a good base for temperature calibrations for past and future concentration measurements with LIF using the same equipment and the gases shown in the tables. It will also be used to see how accurate the thermocouple is to estimate the heating plate temperature. I will thus first discuss the accuracy of the measurements themselves and then how well they may be used to calibrate future measurements.

4.1 Measurement Accuracy

It turned out to more difficult than first anticipated to obtain quantitative temperature measurements due to the laser energy varying between measurements. Since accurate temperature data depends on a difference in intensity between the reference measurement at room temperature and the measurement at the unknown temperature. This especially affects the measurements done at 50 °C where this difference is small. Also, the measurements at 50 °C were usually done early in the measurement series which is when the laser is most unstable. This explains the at times obviously erroneous values below room temperature for the 50 °C measurements.

When comparing the temperatures close to the heating cross at the different pressures one can see that the measurement at 100 mbar shows both higher temperatures as well as a large flow dependence which definitely is outside the margin of error. The higher temperatures may be due to the lower pressure effectively giving the gas a lower heat conductivity since less molecules can transfer heat. This means less heat is transferred from the area around the heating cross to the chamber walls which implies higher temperatures close to the heating cross. The large flow dependence is assumed to be due to the fact that at lower pressures a larger fraction of gas is exchanged at the same flow. At 100 mbar and a flow of 100 ml/min all gas in the 23 ml chamber should be replaced around once every 1.5 s. This can be compared to the measurements at higher

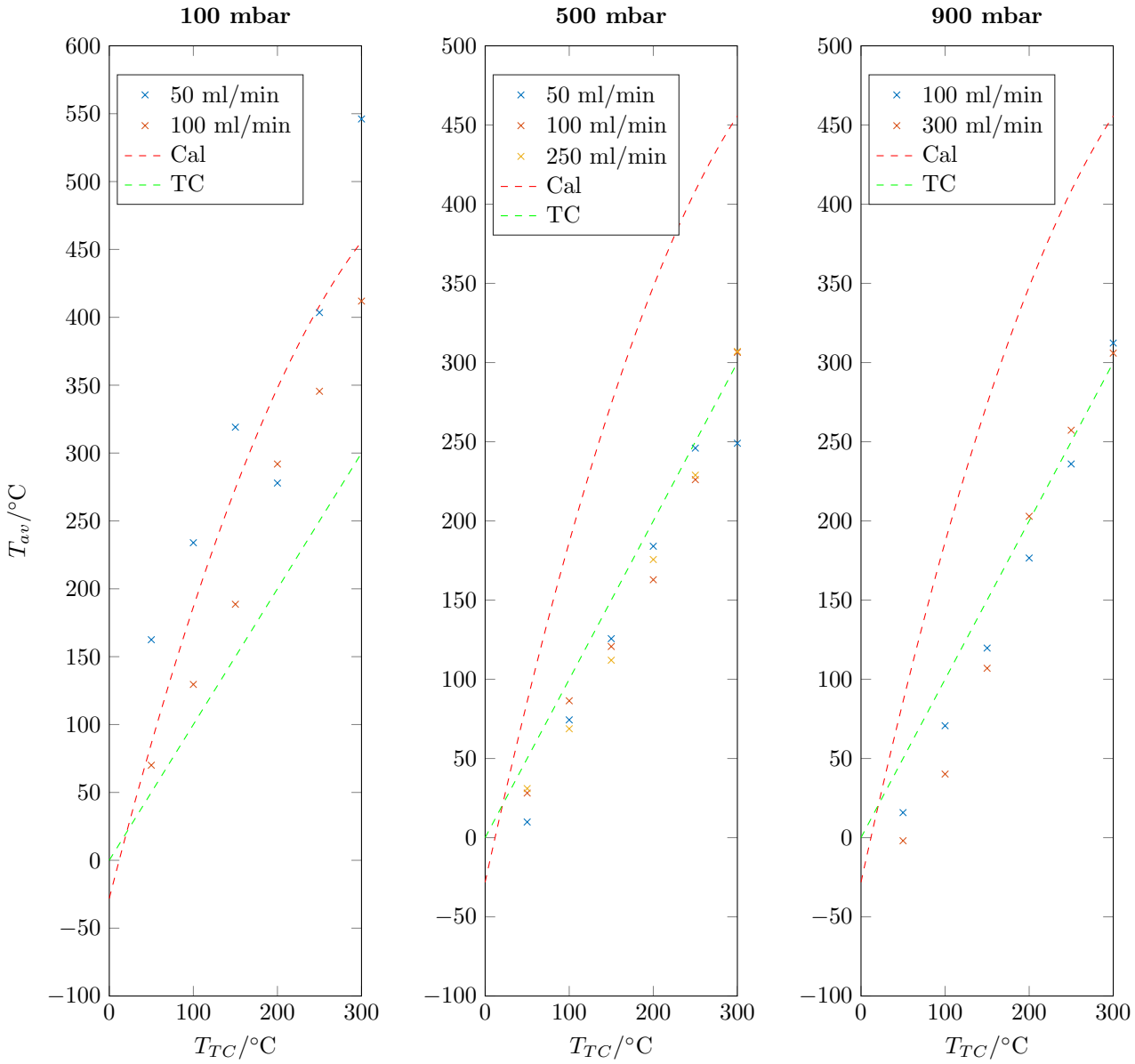

Figure 3: Temperature plots of the average temperature T_{av} of the blue rectangle in figures 4 to 7 as function of the temperature T_{TC} reported by the thermocouple. For reference a linear plot and the calibrated temperature from ESRF ($T_{av} = -0.002671T_{TC}^2 + 2.414T_{TC} - 28.08$) are also plotted.

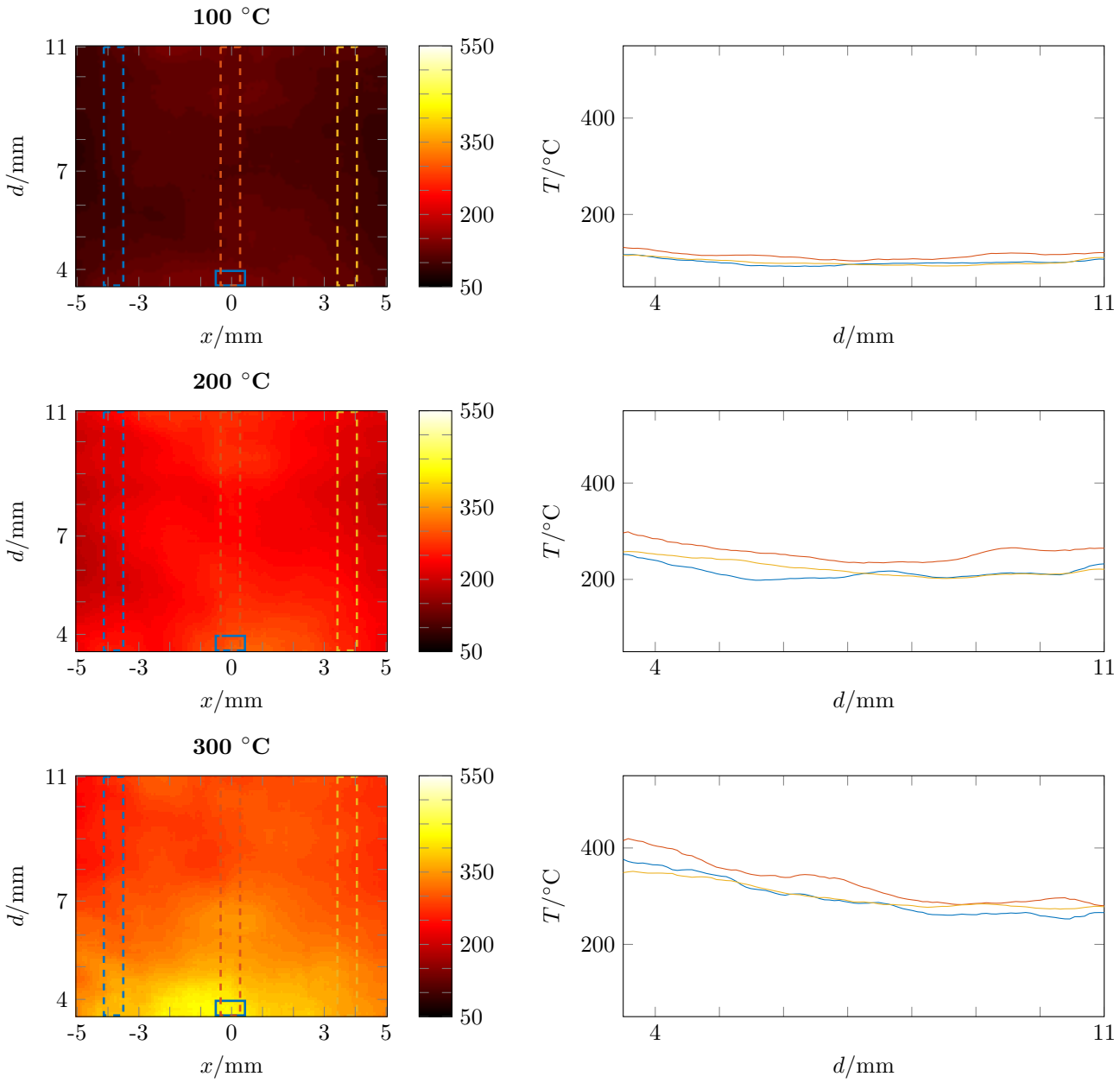

Figure 4: The temperature distribution for 100 °C, 200 °C, 300 °C measured at a flow of 100 ml/min at 100 mbar

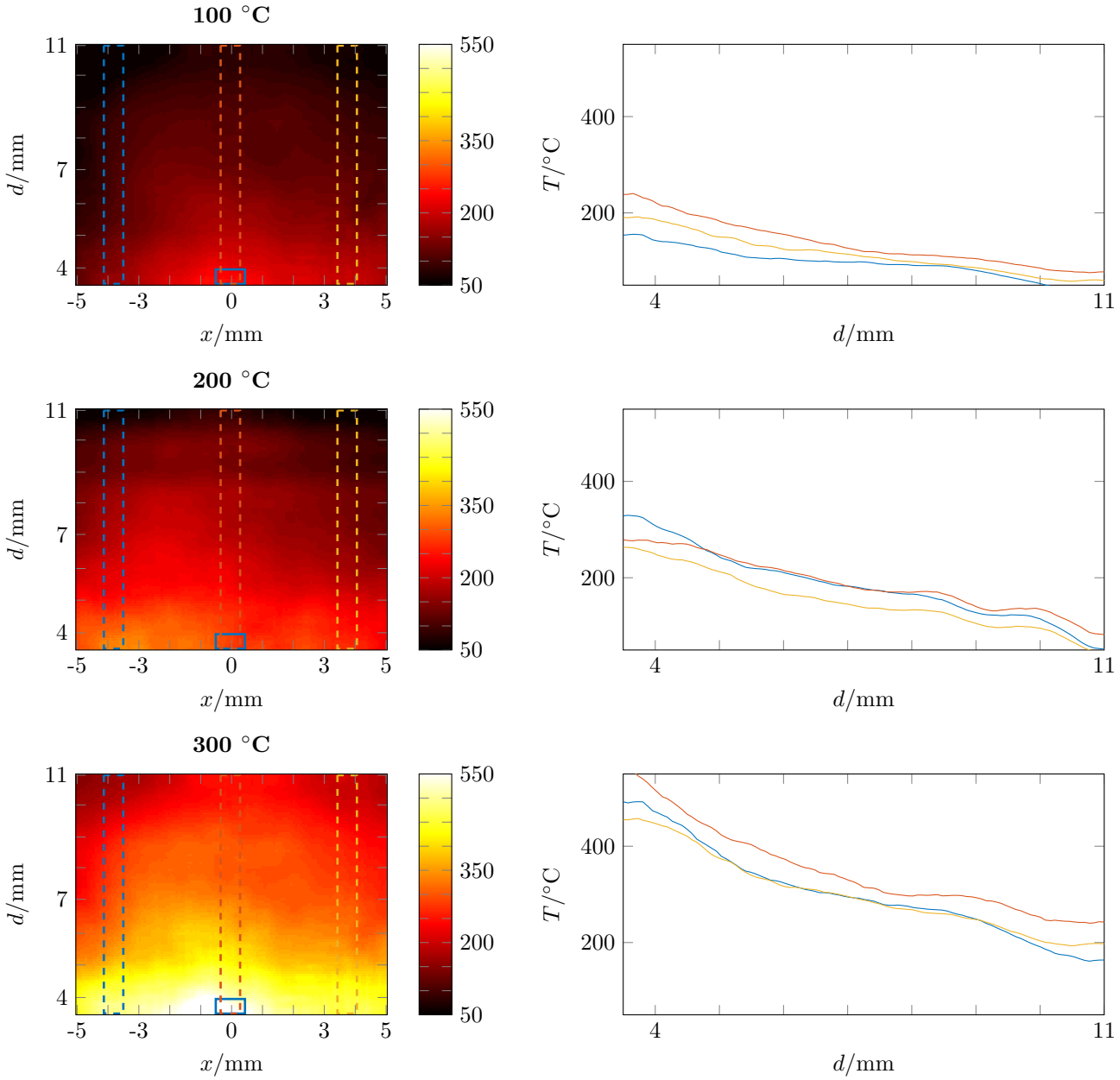

Figure 5: The temperature distribution for 100 °C, 200 °C, 300 °C measured at a flow of 50 ml/min at 100 mbar

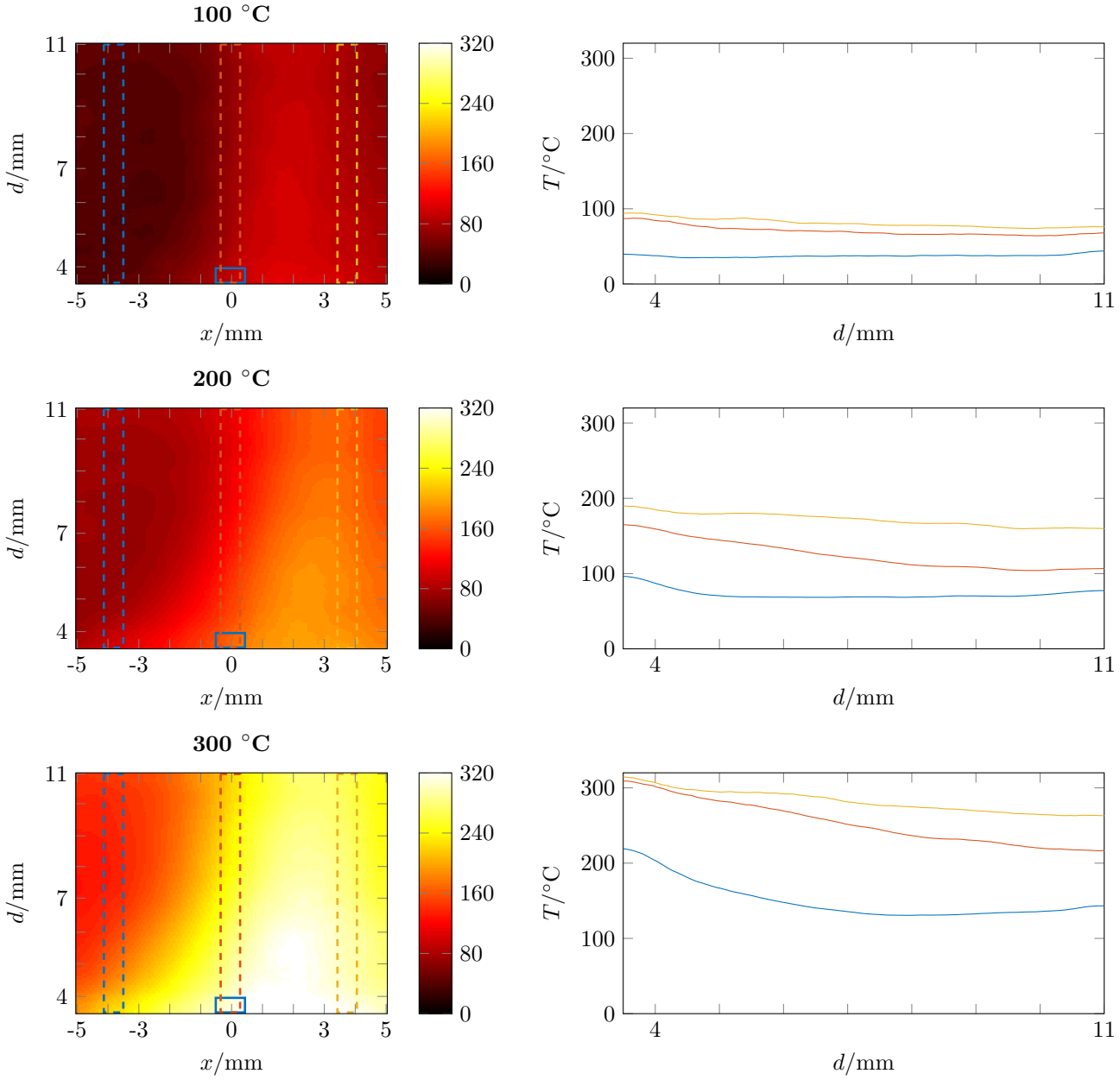

Figure 6: The temperature distribution for 100 °C, 200 °C, 300 °C measured at a flow of 100 ml/min at 500 mbar

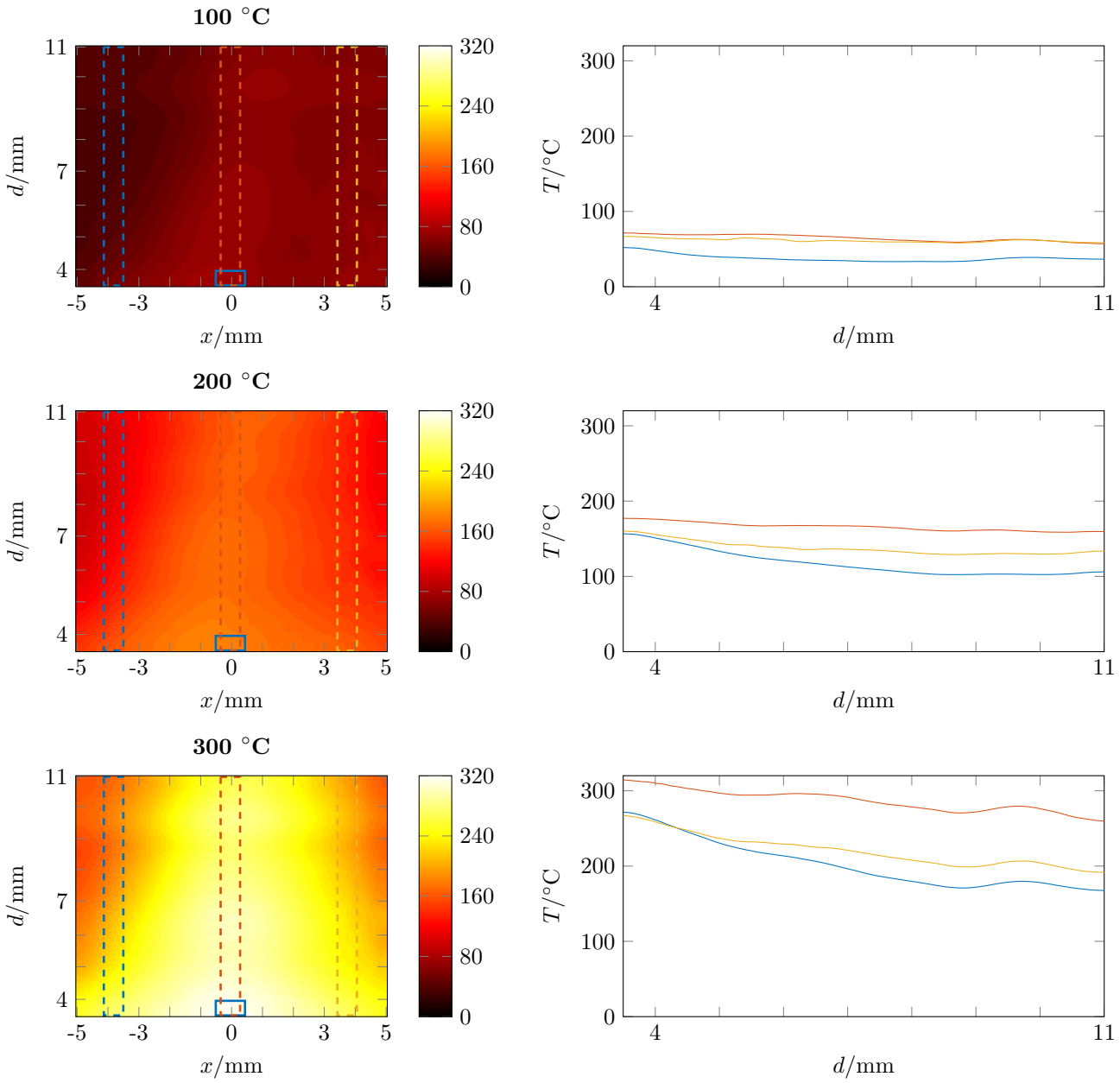

Figure 7: The temperature distribution for 100 °C, 200 °C, 300 °C measured at a flow of 100 ml/min at 900 mbar

pressure, at 900 mbar it takes around 15 s to replace all gas at the same flow rate. This means relatively more cold gas is introduced at lower pressures which leads to a fall in temperature which leads to a large flow dependency. There are no clear patterns of flow dependency at higher pressures which further verifies this claim.

Looking at the temperature maps we can see that most temperature maps are shifted slightly to the right. This is also visible in the line plots; the blue line representing the temperature on the left side is significantly lower than the yellow representing the right side temperature, especially for the larger flows. This is expected since the gas inlet is on the left side, that side should be cooler than the right side which can be seen from the temperature maps. The gas is the hottest in the middle which is right above the heating cross. Comparing the temperature trend plots for 100 ml/min at 500 mbar and 900 mbar one can clearly see that the difference is larger for the 500 mbar map which further verifies the reason for the pressure flow dependency postulated above.

One further source of error may be the dissociation of butane gas used into other components. The two main dissociation paths are $C_4H_{10} \rightarrow C_3H_7 + CH_3$ and $C_4H_{10} \rightarrow 2C_2H_5$ [15]. However, to break the required bonds an energy of around 300 $\mathrm{kJ\,mol^{-1}}$ is required. Even at a temperature as high as 850 K, which is above the experimental conditions by a large margin, only a very small fraction of the butane molecules will be at an energy greater than the bond breaking energy. This gives a reaction rate constant $k = 5.59 \times 10^{-7}\,\mathrm{s^{-1}}$ for the first reaction and $k = 4.21 \times 10^{-7}\,\mathrm{s^{-1}}$ [16]. The smallest fraction of gas is replaced during the 100 ml/min measurement at 900 mbar. Assuming the chamber volume is around 23 ml one can safely assume that most gas has been exchanged after 2 minutes. In theory, at 100 ml/min and a chamber volume of 23 ml the gas should be replaced much faster, around four times per minute. The high estimate of 2 minutes is to make sure even gas trapped in for example vortexes has been replaced. Even if no new gas would be added to the chamber, only around 0.001 % of the butane will have dissociated into other components after 2 minutes. Since none of these components have a very large Rayleigh cross section the effect of dissociation may be considered completely negligible.

These temperature measurements have also been helpful to determine how well the temperature measured by the thermocouple reflects the rectangle temperature. From figure 3 we see that the temperature reported by the thermocouple is below the measured temperature for the measurement done at 100 mbar while it consistently is slightly above the measured temperature for the measurements at higher pressures.

4.2 Usefulness for Calibration

Since the aim of these measurements was to improve temperature calibrations for future measurements it is essential to investigate how well these measurements will be able to fulfil this.

How well these temperature data, assuming the data itself is accurate enough, may be used for other measurements depends on the similarity of the experimental conditions. Since the interest lies mainly in the temperature the two main experimental conditions to be matched are the thermal conductivity of the gases as well as the specific heat capacity. The measurements where these temperature data are used for calibration usually involve gases slightly lighter than butane such as oxygen (O_2), carbon monoxide (CO), carbon dioxide (CO_2) or argon (Ar). Regarding the thermal conductivity it can be seen from table 4 that with an exception for argon and methane, the thermal conductivity of the other gases involved is just slightly lower than that for butane used during the measurements. As discussed in the method section argon was flowed in addition to butane to reach gas flows larger than would have been possible with only butane. However, even if the two gases behave differently the Rayleigh cross section of argon is twenty times lower than that of butane so the minor differences due to the lower thermal conductivity should be negligible.

Moving over to the specific heat capacity it is seen from table 3 that there are significant differences between the gases. More importantly, while all gases except argon due to its single atom nature have a temperature dependent heat capacity, the actual magnitude of the temperature dependence of the specific heat capacity also varies.

So what properties of the temperature distribution does the specific heat capacity affect? For once it affects how quickly cold gas introduced into the chamber is heated. The larger the heat capacity the longer it will take until the new, cold gas is heated. This means that the flow dependency of the data is increased. This would be seen both in the flow dependence of the

Table 3: Specific heat capacities at constant pressure C_p and molar mass M of a few gases for the temperatures relevant to this study [17, 18]. Note the that the heat capacity of argon (Ar) is constant over all temperatures whereas butane (C_4H_{10}) has a strong temperature dependence. The molar masses were determined by looking at a periodic table after which they were rounded to the nearest gram.

Molecule	$C_p/\mathrm{J\,K^{-1}\,mol^{-1}}$				$M/\mathrm{g\,mol^{-1}}$
	300 K	400 K	500 K	600 K	
CO	29.142	29.340	29.792	30.440	28
CO_2	37.220	41.328	44.627	47.327	44
N_2	29.125	29.249	29.580	30.109	28
O_2	29.387	30.109	31.094	32.095	32
Ar	20.786	20.786	20.786	20.786	40
CH_4	35.765	40.631	46.627	52.742	16
C_3H_{10}	73.931	94.014	112.591	128.700	46
C_4H_{10}	101.2	125.3	148.7	169.4	58

Table 4: The thermal conductivity κ for of a few gases for the temperatures relevant to this study [17]. There is a strong temperature dependence, especially for the heavier carbohydrates. However the difference in κ over one temperature stays within an acceptable range.

Molecule	$\kappa/\mathrm{mW\,m^{-1}\,K^{-1}}$			
	300 K	400 K	500 K	600 K
CO	25.0	32.3	39.2	45.7
CO_2	16.8	25.1	33.5	41.6
N_2	26.0	32.3	38.3	44.0
O_2	26.3	33.7	41.0	48.1
Ar	17.9	22.6	26.8	30.6
CH_4	34.1	49.1	66.5	84.1
C_3H_{10}	18.0	30.6	45.5	61.9
C_4H_{10}	16.4	28.4	43.0	59.1

temperature just above the heating plate as well as the difference between the left and right hand side. For a gas with lower thermal conductivity the left side should become warmer as the newly injected cold gas will heat up more rapidly.

An attempt to gauge this difference from the existing data may be done by looking at the flow dependence at different temperatures. Due to the temperature dependency of the specific heat capacity of butane causing it to increase by almost 50 % between 100 °C and 300 °C one would expect some visible traits such as increased flow dependency. Indeed, when comparing the trend plots of the right and left side in the temperature map figures one can see an increase in the splitting between the left and right side temperatures which may be attributed to the change in the specific heat capacity. It is however difficult to judge how the specific heat capacity affects the temperature in any further way.

An interesting note is that while the splitting between the left and the right side increases at higher pressure the temperature dependence of the rectangle temperature T_{rt} decreases as is evident from figure 3. It is unclear as to why this is the case, however it would imply that the rectangle temperature is less flow dependent at higher pressures which means that it by extension should be less dependent on the specific heat capacities of the gases involved. This would mean that temperature maps at higher pressures are more accurate for gases with differing heat capacities.

As may be deduced from table 4 the thermal conductivity for different gases is similar when in the same temperature range, argon and methane being the exceptions. This means that the temperature should be rather accurate

4.3 Error Estimation

The main source of error as discussed in the method section is the fluctuation of the laser energy which is difficult to measure. In an attempt to estimate the error for each measurement we first look at the variations in laser energy over time by comparing the number of counts in the background measurements done during one day of measurements. This is shown in figure 8. It is evident that there is a general decreasing of the laser energy for the first two hours after which it seems to be rather stable. However, during the measurements one consecutive series of temperatures, one reference and once background is measured. The best matching reference is then used. However one series of temperature measurements takes around one hour to complete which means there is a certain discrepancy of the laser energy between the high temperature measurements and the background and room temperature reference measurements, even within the same measurement series. It is assumed that the absolute error introduced by this is around one standard deviation, which gives an absolute error of 263 counts, which implies a relative error of $\approx 2.5\%$. We will henceforth refer to this relative error as ϵ_l.

We also look at the standard deviation within the individual temperature measurements which are assumed to be independent of the long term variations throughout the day. How well this assumptions holds is unclear.

The standard deviation of the data, δ_I and the relative error $\epsilon = \delta_I / I$, within on measurement are shown in figures 9 and 10. As is evident from these images, in the relevant area this error also ranges from 2.0 % in the 50 °C measurement to 2.5 % in the 300 °C measurement. There is a large stripe in the image where the error is significantly larger, it is unclear as to why this is the case. One explanation is that the mode structure of the laser changes over time.

The total absolute error in a temperature image δ_i is calculated by adding up the absolute errors in the raw measurement image δ_{ri} and the background δ_{bg}.

$$\delta_i^2 = \delta_{ri}^2 + \delta_{bg}^2$$

It is worth noting here that the use of SLIPI would have eliminated the background term since both background and data images are captured in a single image. Thus using SLIPI could have reduced the overall error. Then the relative error ϵ_i for both is calculated by dividing the standard deviation δ_I in each point by the intensity I in that point.

$$\epsilon_i = \delta_i / I_i$$

This calculation is performed for both reference and high temperature images. The relative error in the temperature ϵ_T may then be calculated using

$$\epsilon_T^2 = \epsilon_{ht}^2 + \epsilon_{ref}^2 + \epsilon_l^2,$$

where ϵ_{ht} is the error in the high temperature image, ϵ_{ref} is the error in the low temperature reference image and ϵ_l the error caused by the fluctuation of the laser intensity over a longer period of time as mentioned above. To calculate the absolute error in the temperature measurement for a temperature image at temperature T we use

$$\delta_T = \sqrt{\epsilon_T^2} \cdot T,$$

where T is the entire high temperature map for that temperature. Figure 11 shows the absolute errors calculated this way both for at measurement at 50 °C and another one at 300 °C. This error calculation most likely overestimates the error since the all the fluctuations causing constituting the total error most likely are not completely independent. It is however difficult to judge the actual error.

One evident problem is the fact that the absolute error is very large in the rectangle measurement area. This is attributed to the fact that the temperature here is the highest which means the relative error increases due to fewer total counts. Also, since the error is relative, a high temperature further increases the absolute error.

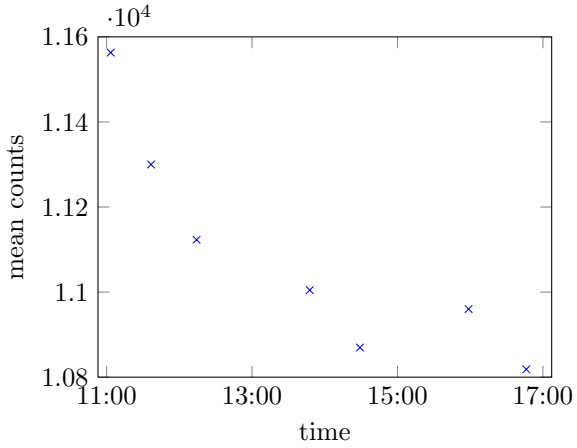

Figure 8: Intensity of the backgrounds measured on 17 Nov. The standard deviation of these values is 263 which at slightly over 10000 counts implies a relative error of around 2.5 %.

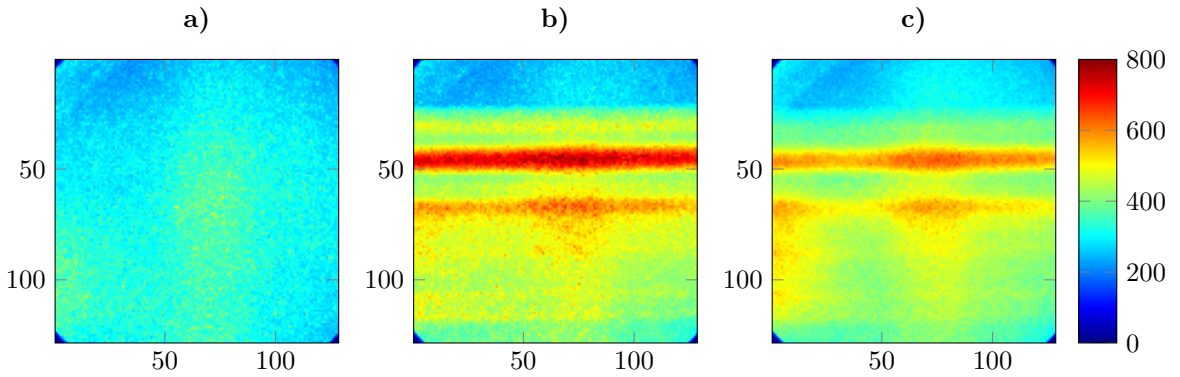

Figure 9: The standard deviation δ_I of a background image (a), an image at 50 °C (b) and an image at 300 °C (c). The top area with no laser sheet which is cut away in the temperature maps is kept in order to show how the laser affects the error.

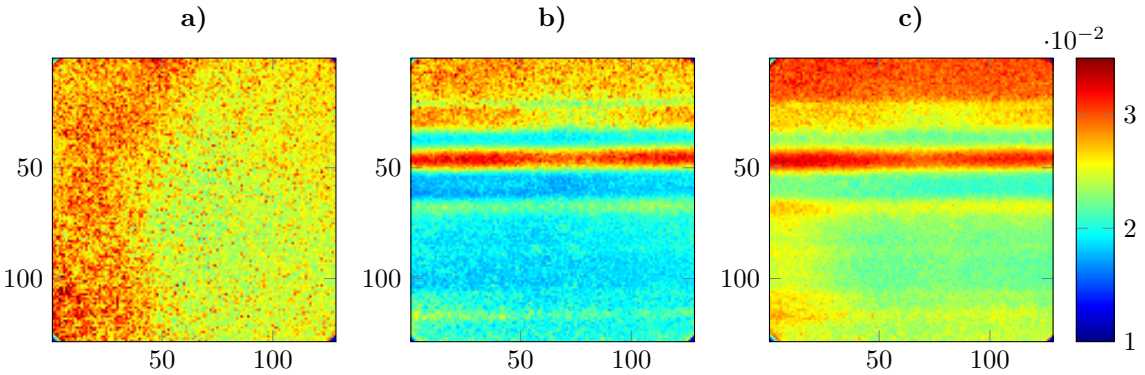

Figure 10: The relative error $\epsilon(= \delta_I/I)$ of a background image (a), an image at 50 °C (b) and an image at 300 °C (c). Note that due to far fewer counts the top quarter, where there is no laser sheet, has a significantly larger relative error due to fewer total counts involved.

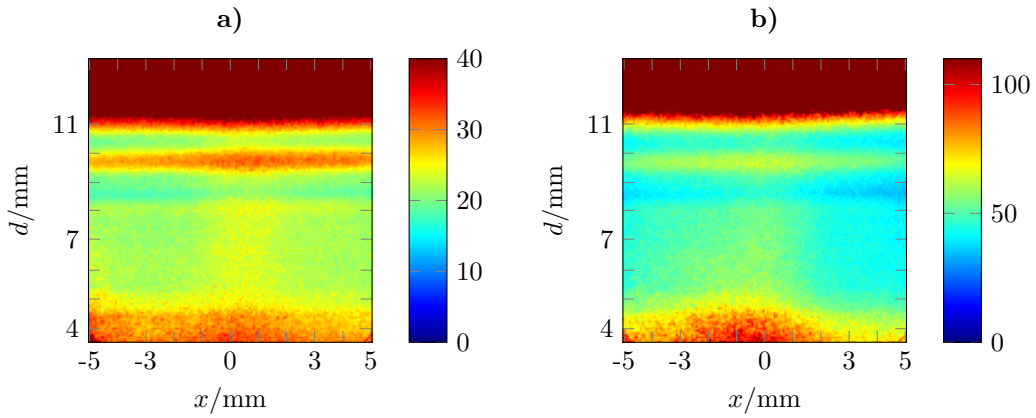

Figure 11: Absolute error δ_T in K of a temperature map at 50 °C (a) and an image at 300 °C (b). Note that the top stripe where the error is huge is outside the laser sheet and thus not relevant for the actual measurements.

5 Conclusion

We have successfully created temperature maps of the reaction test chamber used. We have also created plots of the temperature in the area just above the heating cross which is the main area of interest at various pressures. These plots show that the temperature reported from the thermocouple is slightly erroneous for larger pressures. The calibration provided by ESRF is more correct for lower pressures.

It would be interesting to fully perform similar measurements using the SLIPI technique for background subtraction. As discussed this should decrease the error due to laser fluctuations since each data point would require two less images.

If the error in the temperature is indeed as large as calculated it could limit the use of the temperature maps for the calibration of other measurements. Further investigation to estimate the error more accurately is thus needed. As discussed, independent of the error in the actual measurement, other measurements will use other gases which means the usability of these temperature data will depend on the specific details such as what flows, gases and pressures are used. Nonetheless, assuming the error is small enough these measurements will be of great help to calibrate future catalyst measurements using the same test chamber and gas flow equipment.

Acknowledgements

I would like to thank my supervisors Johan Zetterberg and Jianfeng Zhou for the support they have provided throughout the project.

References

[1] G. Ertl, H. Knozinger, F. Schuth, and J. Weitkamp, "Handbook of heterogeneous catalysis, 2nd edition," 2008.

[2] G. A. Somorjai and Y. Li, *Introduction to surface chemistry and catalysis*. John Wiley & Sons, 2010.

[3] H. Over, Y. Kim, A. Seitsonen, S. Wendt, E. Lundgren, M. Schmid, P. Varga, A. Morgante, and G. Ertl, "Atomic-scale structure and catalytic reactivity of the ruo," 2000.

[4] B. Hendriksen and J. Frenken, "Co oxidation on pt (110): scanning tunneling microscopy inside a high-pressure flow reactor," *Physical Review Letters*, vol. 89, no. 4, p. 046101, 2002.

[5] R. W. Sidwell, H. Zhu, R. J. Kee, D. T. Wickham, C. Schell, and G. S. Jackson, "Catalytic combustion of premixed methane/air on a palladium-substituted hexaluminate stagnation surface," *Proceedings of the Combustion Institute*, vol. 29, no. 1, pp. 1013–1020, 2002.

[6] R. W. Sidwell, H. Zhu, R. J. Kee, and D. T. Wickham, "Catalytic combustion of premixed methane-in-air on a high-temperature hexaaluminate stagnation surface," *Combustion and flame*, vol. 134, no. 1, pp. 55–66, 2003.

[7] J. L. Kinsey, "Laser-induced fluorescence," *Annual Review of Physical Chemistry*, vol. 28, no. 1, pp. 349–372, 1977.

[8] R. B. Miles, W. R. Lempert, and J. N. Forkey, "Laser rayleigh scattering," *Measurement Science and Technology*, vol. 12, no. 5, p. R33, 2001.

[9] E. Berrocal, E. Kristensson, M. Richter, M. Linne, and M. Aldén, "Application of structured illumination for multiple scattering suppression in planar laser imaging of dense sprays," *Optics express*, vol. 16, no. 22, pp. 17870–17881, 2008.

[10] J. Zetterberg, S. Blomberg, J. Gustafson, Z. Sun, Z. Li, E. Lundgren, and M. Aldén, "An in situ set up for the detection of co2 from catalytic co oxidation by using planar laser-induced fluorescence," *Review of Scientific Instruments*, vol. 83, no. 5, p. 053104, 2012.

[11] J. A. Sutton and J. F. Driscoll, "Rayleigh scattering cross sections of combustion species at 266, 355, and 532 nm for thermometry applications," *Optics letters*, vol. 29, no. 22, pp. 2620–2622, 2004.

[12] O. Svelto, *Principles of lasers*. Springer, 2010.

[13] C. Johnson, "Optimal placement of apertures in optical setups," *Enrichment Center Letters*, 1949. Aperture Science Laboratories.

[14] *Landolt-Börnstein, Zahlenwerte und Funktionen aus Physik, Chemie, Astronomie, Geophysik, und Technik. Sechste Auflage.*, vol. 2. Springer, 1962.

[15] Y. L. Wang, *I. Thermal decomposition of N-butane. II. Flow in entrance section of parallel plates*. PhD thesis, California Institute of Technology, 1963.

[16] K. M. Sundaram and G. F. Froment, "Modeling of thermal cracking kinetics. 3. radical mechanisms for the pyrolysis of simple paraffins, olefins, and their mixtures," *Industrial & Engineering Chemistry Fundamentals*, vol. 17, no. 3, pp. 174–182, 1978.

[17] D. R. Lide, *CRC handbook of chemistry and physics*. CRC press, 2004.

[18] B. Younglove and J. F. Ely, "Thermophysical properties of fluids. ii. methane, ethane, propane, isobutane, and normal butane," *Journal of Physical and Chemical Reference Data*, vol. 16, no. 4, pp. 577–798, 1987.